

# Doppler-free, Multi-wavelength Acousto-optic deflector for two-photon addressing arrays of Rb atoms in a Quantum Information Processor

Sangtaek Kim,<sup>1,\*</sup> Robert R. Mcleod,<sup>1</sup> Mark Saffman,<sup>2</sup> and Kelvin H. Wagner<sup>1</sup>

<sup>1</sup>Optoelectronic Computing Systems Center,  
Department of Electrical & Computer Engineering,  
University of Colorado at Boulder, Boulder, CO

<sup>2</sup>Department of Physics, University of Wisconsin, Madison, WI

\* Corresponding author: sangtaek@colorado.edu

February 2, 2008

## Abstract

We demonstrate a dual wavelength acousto-optic deflector (AOD) designed to deflect two wavelengths to the same angles by driving with two RF frequencies. The AOD is designed as a beam scanner to address two-photon transitions in a two-dimensional array of trapped neutral  $^{87}\text{Rb}$  atoms in a quantum computer. Momentum space is used to design AODs that have the same diffraction angles for two wavelengths (780 nm and 480 nm) and have non-overlapping Bragg-matched frequency response at these wavelengths, so that there will be no crosstalk when proportional RF frequencies are applied to diffract the two wavelengths. The appropriate crystal orientation, crystal shape, transducer size, and transducer height are determined for an AOD made with a Tellurium dioxide crystal ( $\text{TeO}_2$ ). The designed and fabricated AOD has more than 100 resolvable spots, widely separated bandshapes for the two wavelengths within an overall octave bandwidth, spatially overlapping diffraction angles for both wavelengths (780 nm and 480 nm), and a 4  $\mu\text{sec}$  or less access time. Cascaded AODs in which the first device upshifts and the second downshifts allow Doppler-free scanning as required for addressing the narrow atomic resonance without detuning. We experimentally show the diffraction-limited Doppler-free scanning performance and spatial resolution of the designed AOD.

## 1 Introduction

Quantum algorithms may provide large gains in computational speed for certain problems such as factoring or database searching.<sup>1-3</sup> Operation of quantum gates and execution of small quantum algorithms have been demonstrated using several different physical embodiments of quantum logic including nuclear magnetic resonance, cold trapped ions, single

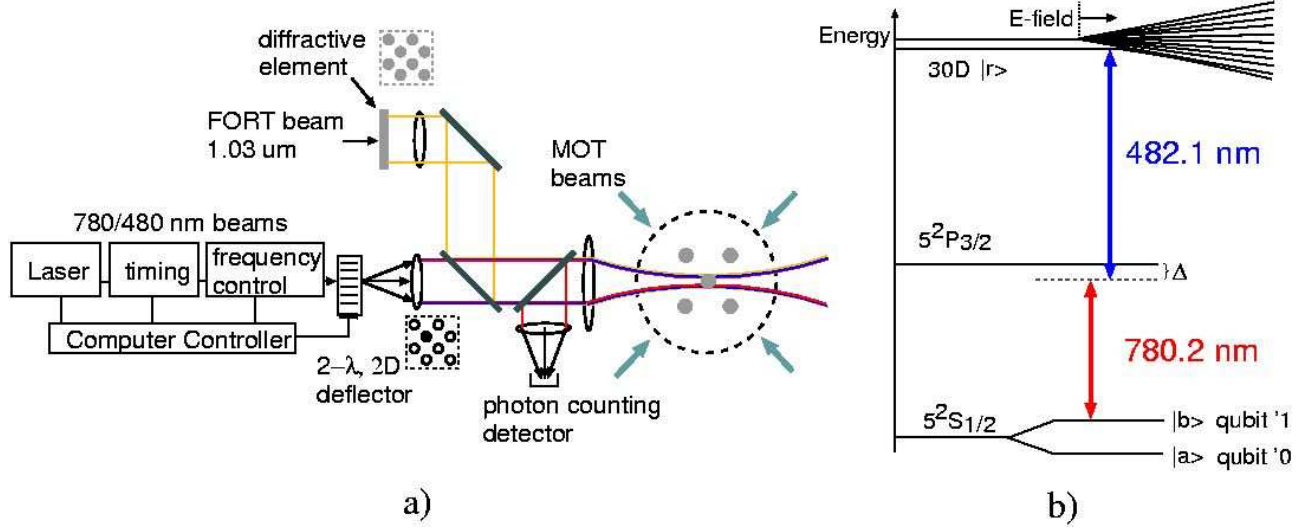


Figure 1: a) Rydberg atom quantum processor with two-dimensional array of trapped atoms, b) Two-level Rydberg excitation using two wavelengths (780 nm/480 nm).

photons, and superconducting circuits.<sup>4–7</sup> The current challenge in experimental quantum computing is the task of scaling to larger numbers of qubits and logical operations. One of the implementations which appears particularly attractive because of its potential scalability is to use an array of neutral atoms trapped in optical lattices. Using well developed techniques of laser cooling and trapping, it is possible to create arrays of optical trapping sites and load them with single neutral atoms as shown in Figure 1 a). Long lived qubits can then be encoded in different hyperfine atomic ground states. Single qubit operations can be performed by stimulated transitions induced by laser beams focused on individual sites, or by Zeeman addressing.<sup>8–10</sup> Several different physical mechanisms can potentially be used for two-qubit operations including collisions and dipole-dipole interactions.<sup>11,12</sup> High lying Rydberg levels with principal quantum number  $n$  have dipole moments which scale as  $n^2ea_0$  where  $e$  is the electronic charge and  $a_0$  is the Bohr radius. Dipole-dipole interactions of Rydberg atoms therefore scale as  $n^4e^2a_0^2/r^3$ , with  $r$  the atomic separation. A detailed analysis of quantum gates using Rydberg interactions predicts the feasibility of high fidelity operations at MHz rates between optically resolvable sites by exciting Rydberg levels with  $n \sim 70$ .<sup>13</sup>

A peculiarity of the Rydberg scheme is that because the two-atom interaction utilizes excited states which have a finite radiative lifetime there is an optimum speed for which the gate fidelity is maximized. If the gate is run too slow radiative decay from the Rydberg states will lead to large errors, and if the gate is run too fast the dipole-dipole interaction will not be strong enough to provide the desired logical operation. Analysis predicts<sup>13</sup> that gate speeds of several MHz, corresponding to sub-microsecond access times for individual qubits will be optimal. Furthermore, transitions from the ground state to high lying Rydberg levels of alkali atom are in the deep UV spectral region where the unavailability and immaturity of lasers, modulators, detectors, and other optical technologies is inconvenient. A convenient technological alternative is to use a two-photon transition, which is resonantly enhanced by an intermediate level. For example in <sup>87</sup>Rb ground to Rydberg transitions can be reached

efficiently using a 780 nm laser that is near resonant with the  $5s_{1/2} \rightarrow 5p_{3/2}$  transition followed by a 480 nm laser coupling to a Rydberg level such as  $5p_{3/2} \rightarrow ns_{1/2}$  or  $5p_{3/2} \rightarrow nd_{3/2,5/2}$  as shown in Figure 1 b). Two-photon Rabi oscillations between ground and Rydberg states using this approach have recently been demonstrated with single atoms in optical traps.<sup>14</sup>

In light of the above considerations, implementation of a quantum processor based on a two-dimensional array of trapped atoms interacting via Rydberg states requires a fast beam scanner that provides  $\mu\text{s}$  access times for two different wavelengths. The required scanner specifications are that the output beam positions have to overlap for both wavelengths (780 nm and 480 nm), no Doppler shift of the sum of the two frequencies is tolerable (to avoid detuning of the two-photon transition), and the access time should be less than a few micro-seconds. The number of qubits that can be addressed will be fixed by the number of resolvable spots of the scanner. Several different beamsteering technologies can be considered for this application. Liquid crystal beam deflectors have millisecond scale access time, which is too slow.<sup>15</sup> Electro-optic prism beam deflectors are theoretically fast enough but require such high voltages that their speed is limited by the drive electronics to the millisecond range.<sup>16</sup> MEMS mirrors are attractive since they work for both wavelengths without any Doppler shift, but sufficiently high-resolution beamsteering requires large apertures and deflection angles, which require milli-second response times, and are thus also too slow.<sup>17</sup> A recent paper by Kim<sup>18</sup> demonstrated a MEMS mirror with 11  $\mu\text{s}$  switching time between two sites, but this would be slower for addressing larger arrays. Acousto-optic deflectors (AODs) produce unwanted Doppler shifts but have advantages in terms of access time and resolution and can be crossed to scan two-dimensional arrays. The Doppler shift can be canceled by cascading two AODs with opposite diffraction orders<sup>19</sup> or by pre-compensation with a double-passed AOD that produces Doppler without any angular deflection. AODs are thus good candidates for two-dimensional, multi-color addressing because of their high access speed; however, the problems of Doppler shift and the difference of diffraction angles with wavelength are problems that must be solved to make use of AODs for this quantum information processing (QIP) application of two-color addressing of two-dimensional arrays of trapped atoms. This paper describes the design and development of a high-speed, high-efficiency, Doppler-free, multi-beam and multi-color acousto-optic scanner system usable in QIP applications to rapidly address arrays of trapped atoms. This type of device may also be of interest for other implementations of quantum logic such as trapped ions, superconductors, or quantum dots in semiconductors.

## 2 Background on Acousto-optic devices

AODs consist of piezoelectric transducers bonded onto bulk photoelastic crystals such as  $\text{TeO}_2$ . Applying RF electrical signals to the transducer launches bulk acoustic waves into the crystal, periodically modulating the crystal's dielectric tensor or index of refraction with a traveling wave. The modulation of the index of refraction functions as a volume index grating, which diffracts collimated light incident on the AOD at the Bragg angle. The diffraction angle,  $\theta \approx \frac{\lambda}{\Lambda} = \frac{\lambda f}{V_a}$ , is proportional to the applied RF frequency,  $f$ , and inversely proportional to the acoustic velocity,  $V_a$ , of the AOD. The scan angle is also proportional to the optical wavelength  $\lambda$ , so the scan angles vary from  $\theta_1 \approx \frac{\lambda_1 f}{V_a}$  to  $\theta_2 \approx \frac{\lambda_2 f}{V_a}$  for two

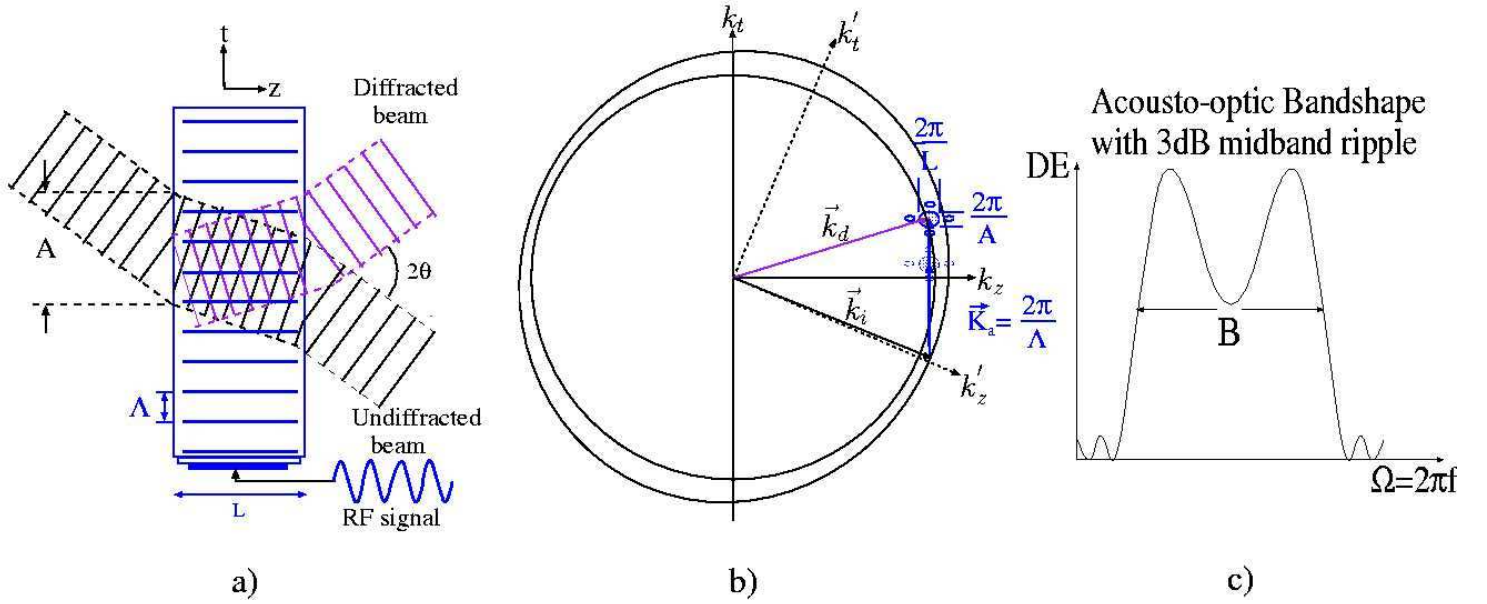


Figure 2: a) Real-space view of acousto-optic diffraction. A single frequency applied RF signal produces a sinusoidal grating inside the AO medium, which diffracts the incident plane wave with an angle  $2\theta$ . b) Momentum space representation of acousto-optic diffraction for an acoustically and optically rotated  $\text{TeO}_2$  device. As the frequency increases, the coupling efficiency between the uncertainty distribution and optical momentum surface gives the RF bandshape of the AOD. c) The acousto-optic bandshape with slight angle detuning gives the 3 dB ripple bandshape.

different wavelengths given a fixed RF frequency. The wavelength-dependent scan angle of the AOD can be compensated by applying two RF frequencies simultaneously with the ratio of frequencies determined by the wavelengths ( $\frac{f_1}{f_2} = \frac{\lambda_2}{\lambda_1}$ ), so that each wavelength is diffracted into the same direction by the corresponding proportional RF frequency.

The number of resolvable spots of an AOD is given by time-bandwidth product ( $N = T \cdot B$ ), where  $T = A/V_a$  is the acoustic propagation time across the device aperture  $A$ , and  $B$  is the bandwidth limited by the transducer acousto-electric conversion bandwidth and the Bragg-matched bandwidth, so one should be able to achieve better resolution with larger bandwidth AOD. However, since the acoustic attenuation increases with frequency as  $\alpha = \alpha_0 f^2$ , the limiting device aperture decreases with frequency squared, thus the number of resolvable spots actually decreases with increasing frequency, so a better strategy is to lower the frequency to increase the  $T \cdot B$  as long as a sufficiently large crystal is available. The acoustic velocity  $V_a$  and the area of the beam incident on the AOD,  $A$ , determine the access time  $T = \frac{A}{V_a}$  and resolution  $N = \frac{A \cdot B}{V_a}$ . Thus AO-addressing speed must be traded off with resolution.

As shown in Figure 2, we can describe the diffraction of an AOD in momentum space (Fourier space), which provides a graphical picture of the acousto-optic interaction for our AOD design in the small diffraction efficiency limit (Born approximation). The Born approximation simplifies complex coupled-mode problem to linear equations allowing the use of graphical momentum space design techniques for optimizing the acousto-optic interaction

geometry, even though in application we will use the devices with much higher diffraction efficiency.<sup>20</sup>

The simplest description of the requirement for the conservation of momentum in acousto-optic diffraction requires the closure of the triangle of the input optical wavevector,  $\vec{k}_i$  (which lies on the optical momentum surface), with the acoustic grating wavevector,  $\vec{K}_a$ , to give the output optical wavevector,  $\vec{k}_d$ . Often, slight deviations from perfect momentum matching are attributed to momentum mismatch  $\Delta\vec{K}$  describing the deviation of  $\vec{k}_i + \vec{K}_a$  from  $\vec{k}_d$ .<sup>21</sup> Instead, to account for slight allowable momentum mismatch in finite media, we introduce the concept of momentum uncertainty, given by the 3-D Fourier transform of the interaction region and enforce the requirement that the diffracted field is a superposition of plane wave components lying on the optical momentum surface.<sup>20,22</sup> The convolution of the 3-D Fourier transform of the incident optical field with the dielectric perturbation caused by the acoustic wave launched by the transducer (acoustic grating) sampled by the  $\vec{k}$ -sphere of the allowed propagating eigenmodes represents the angular spectrum of the diffracted optical wave. When the transducer is driven by frequency  $\Omega$ , it launches a bulk acoustic wave causing a time-varying impermeability tensor

$$\begin{aligned} \Delta_{\underline{\underline{\eta}}}(\vec{r}, t) = & \frac{1}{(2\pi)^2} \int \int_{\underline{\underline{\eta}}} p \hat{S}(K_y, K_z) (\underline{\underline{S}}_T \cdot \hat{S}(K_y, K_z)) A(K_y, K_z) \\ & \times \frac{1}{2\pi} \int R(\Omega) \exp[i(\Omega t - (\sqrt{[\Omega/V_a(K_y, K_z)]^2 - K_y^2 - K_z^2} x + K_y y + K_z z))] d\Omega dK_y dK_z, \end{aligned} \quad (1)$$

where  $p$  is the photoelastic tensor,  $\hat{S}(K_y, K_z)$  is the directional-dependent acoustic strain polarization tensor while  $\underline{\underline{S}}_T$  is the strain polarization produced by the transducer,  $R(\Omega)$  is the Fourier transform of the applied RF signal,  $A(K_y, K_z)$  is the Fourier transform of the transducer aperture function,  $a(y, z)$ . In the case of  $\text{TeO}_2$  crystal,  $\hat{S}(K_y, K_z)$  is approximately equal to [110] for all directions near [110], so that  $\underline{\underline{S}}_T \cdot \hat{S}(K_y, K_z)$  is approximately equal to 1. The dielectric tensor perturbation is given by

$$\Delta_{\underline{\underline{\epsilon}}}(\vec{r}, t) = \underline{\underline{\epsilon}} \Delta_{\underline{\underline{\eta}}}(\vec{r}, t) \underline{\underline{\epsilon}}, \quad (2)$$

where  $\underline{\underline{\epsilon}}$  is the permittivity tensor. We can represent the angular spectrum of the diffracted  $E_d(\vec{r}, t)$  optical wave as:

$$E_d^{\omega_d}(k_x, k_y, L) = \frac{i\omega_d^2}{2c^2 k_{zd}^q(k_x, k_y)} \int \delta(k_z - k_{zd}^q(k_x, k_y)) \mathcal{F}_{\vec{r}} \left\{ \Delta_{\underline{\underline{\epsilon}}}(\vec{r}, \Omega) \vec{E}_i^*(\vec{r}, \omega) \right\} \cdot \hat{p}_q(k_x, k_y) dk_z \quad (3)$$

where  $c$  is the velocity of light,  $L$  is the crystal interaction length (transducer length),  $k_{zd}^q(\vec{k}_t) = \sqrt{k_d^2 - |\vec{k}_t|^2}$  is the longitudinal component of the diffracted wavevector solved from an eigenvalue problem for the homogeneous crystal with corresponding polarization eigenvectors  $\hat{p}_q(k_x, k_y)$  for the two allowed modes.  $k_d = 2\pi n_d(\vec{k}_t, \omega_d) \omega_d / c$  describes the anisotropic magnitude of the diffracted wavevector,  $\vec{k}_t = \hat{x}k_x + \hat{y}k_y$  is the transverse component of the wavevector, and  $\vec{E}_i(\vec{r}, \omega)$  is the incident optical field at the crystal boundary with optical frequency  $\omega$ . The Doppler shift of the diffracted beam is given by the conservation of energy

$\omega_d = \omega \pm \Omega$  corresponding to Doppler upshifting (+) and downshifting (-) orders. In this expression, the 3-D Fourier transform of the product of the incident field and the dielectric perturbation is sampled by the delta function representing the momentum surface of allowed propagating modes, which give the source term for the angular spectrum of the diffracted field at the output of AO medium.

We use momentum space (or  $\vec{k}$ -space) as summarized by Equation 3 to design the dual-wavelength AODs required for this QIP application. When the piezoelectric transducer launches an acoustic wave, a grating is produced through the photoelastic effect. The grating is represented in  $\vec{k}$ -space as a grating vector whose length  $|\vec{K}_a| = \Omega/V_a$  with an uncertainty distribution at its tip due to the finite extent of the acoustic wave, where  $\Omega$  is the angular radian RF frequency. We can regard the propagating acoustic wave as a moving grating with frequency  $\Omega$  (grating period  $\Lambda = 2\pi V_a/\Omega$ ) and grating width  $L$  (given by the transducer length). The incident electric field ( $E_i(\vec{r}, \omega)$ ) has Bragg-matched wavevector  $|\vec{k}_i| = \frac{2\pi n_i}{\lambda}$  and we approximate its envelope as a rectangle of width  $A$  in the  $t$  direction, as shown in Figure 2 a). As shown by the term in braces in Equation 3, the real-space product of the dielectric perturbation  $\Delta\epsilon(\vec{r}, \Omega)$  and the incident electric field yields the material polarization that has a rectangular profile of  $A \times L$  as shown in Figure 2 a). Its Fourier transform is therefore a product of sinc function of width  $2\pi/A \times 2\pi/L$  displaced from the origin by a carrier  $\vec{k}_i + \vec{K}_a$ , as shown in Figure 2 b). This Fourier uncertainty distribution represents the acousto-optically induced polarization responsible for diffracting the optical field as represented in momentum space. The uncertainty distribution is illustrated as a single contour line, which is the product of sinc functions rendered in momentum space shown in Figure 2 b). In general, this uncertainty distribution is represented with a 3-D Fourier transform of the product of the incident optical wave and acoustic field amplitude. The angular distribution of the diffracted field is then found by sampling this uncertainty distribution with the allowed propagating eigenmode as shown in Equation 3 and Figure 2 b). When the RF frequency  $\Omega = 2\pi f$  is applied, the acoustic momentum  $\vec{K}_a$  linearly increases and tangentially skims along the diffracted optical momentum surface with slight angular detuning. The acousto-optic bandshape versus applied RF frequency can be found geometrically in momentum space as the overlap of the uncertainty distribution with the allowed propagating eigenmodes as illustrated in Figure 2 b). The resulting 3 dB rippled acousto-optic bandshape is as illustrated in Figure 2 c).<sup>20,23</sup>

For our AOD beam scanner design, we chose  $\text{TeO}_2$  as our AO crystal because of its anomalous slow shear mode with high diffraction efficiency and high resolution when compared to other crystals (e.g., GaP or  $\text{LiNbO}_3$ ).<sup>24</sup> Using the stiffness tensor coefficients of the  $\text{TeO}_2$  crystal, the directional dependent acoustic velocity can be determined from the eigensolution of the Christoffel equation.<sup>25,26</sup> The inverse velocity, or slowness surface, is shown in Figures 3 a) and b). Along the [110] directions, the velocity of the shear wave polarized in the  $\bar{X}\bar{Y}$  plane (0.62 mm/ $\mu$ sec) is nearly 10 times slower than in conventional AO crystals. The slow acoustic velocity of  $\text{TeO}_2$  gives a high figure of merit  $M_2 = (n^6 p^2)/(\rho V_a^3)$  ( $n$  is refractive index,  $p$  is the photo-elastic constant,  $\rho$  is the material density) which is the key material parameters that determines acousto-optic diffraction efficiency  $\eta$ .

$$\eta \equiv \frac{I_d}{I_0} = \sin^2 \left[ \frac{\pi^2 P_a L}{2\lambda^2 H} M_2 \right]^{1/2}, \quad (4)$$

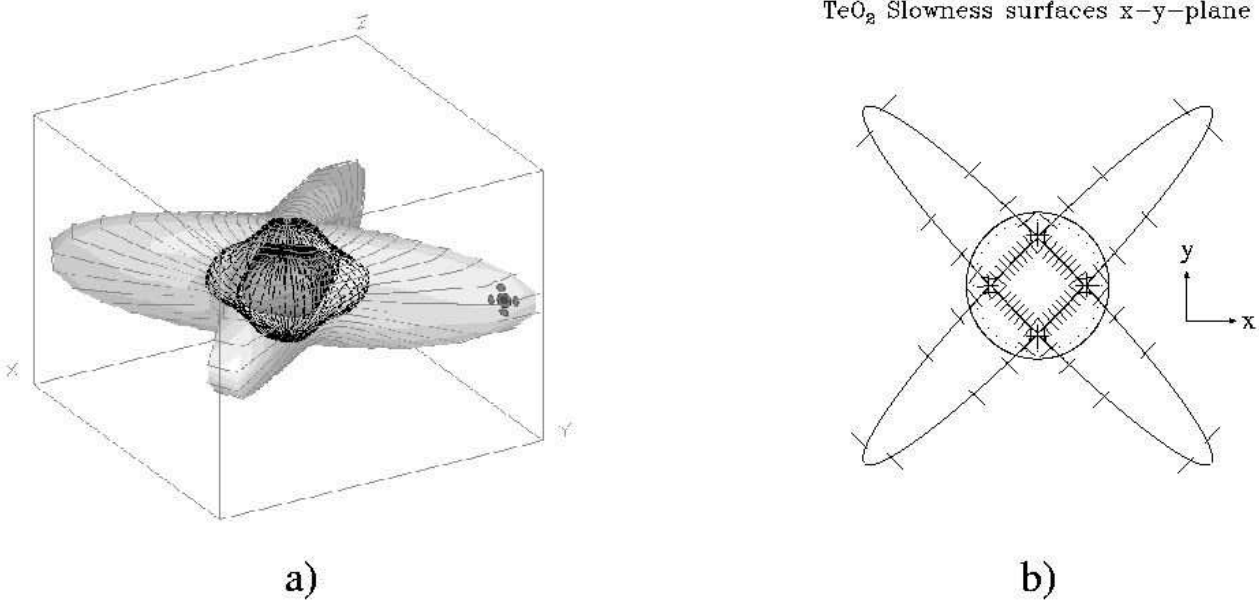


Figure 3: a) Three-dimensional TeO<sub>2</sub> slowness surfaces with 3 different acoustic polarizations and the transducer Fourier transform  $P(K_y, K_z)$  projected onto the surface for an acoustically rotated geometry.<sup>22</sup> b) Top view of TeO<sub>2</sub> slowness surface. Along [110], the acoustic velocity is extremely slow which results in high diffraction efficiency. The indicated slow shear wave acoustic polarization remains nearly constant as the propagation direction deviates from [110].

where  $P_a$  is the acoustic power,  $H$  is the transducer height, and  $L$  is the transducer length. The slow velocity of TeO<sub>2</sub> not only yields high  $M_2$  and high efficiency, but also enables high resolution and large angular diffraction at moderate drive frequencies that yield large time-bandwidth product operation. However, the large acoustic attenuation of 18 dB/ $\mu\text{s}\cdot\text{GHz}^2$ , the slow access speed, and the large walk-off angles for acoustically rotated devices present challenges to the use of this slow-shear mode in TeO<sub>2</sub>.<sup>24–26</sup>

The acoustic walk-off angle is determined by the tilt of the acoustic slowness surface relative to the acoustic grating vector ( $\vec{K}_a$ ). Second and higher-order terms in the Taylor expansion of the slowness surface represent acoustic diffraction. This diffraction is quantified by the Rayleigh-range that indicates the well-collimated region (distance  $Z_0$ ) of the diffracting wave, which is defined as

$$Z_0 = \frac{D^2}{b\Lambda_a}, \quad (5)$$

where  $D$  is the spatial width of propagating wave,  $\Lambda_a$  is the wavelength, and  $b$  is inverse of the slowness surface radius of curvature relative to an isotropic material.<sup>22</sup> For an acoustic wave propagating along the [110] direction in TeO<sub>2</sub> crystal, the diffracting power (or excess curvature) in  $z - xy$  plane ( $b_z$ ) is 11, and 52 for the  $xy(b_t)$  plane. The walk-off angle can be approximately given by  $b \cdot \theta$  for small  $\theta$ , where  $\theta$  is the angle between the acoustic wave propagation direction and the symmetry axis direction ([110] in TeO<sub>2</sub>).<sup>26</sup>

TeO<sub>2</sub> is a positive uniaxial crystal with a slight splitting between the eigen surfaces along the z-axis due to optical activity. This splitting of the eigen surfaces allows tangential bire-

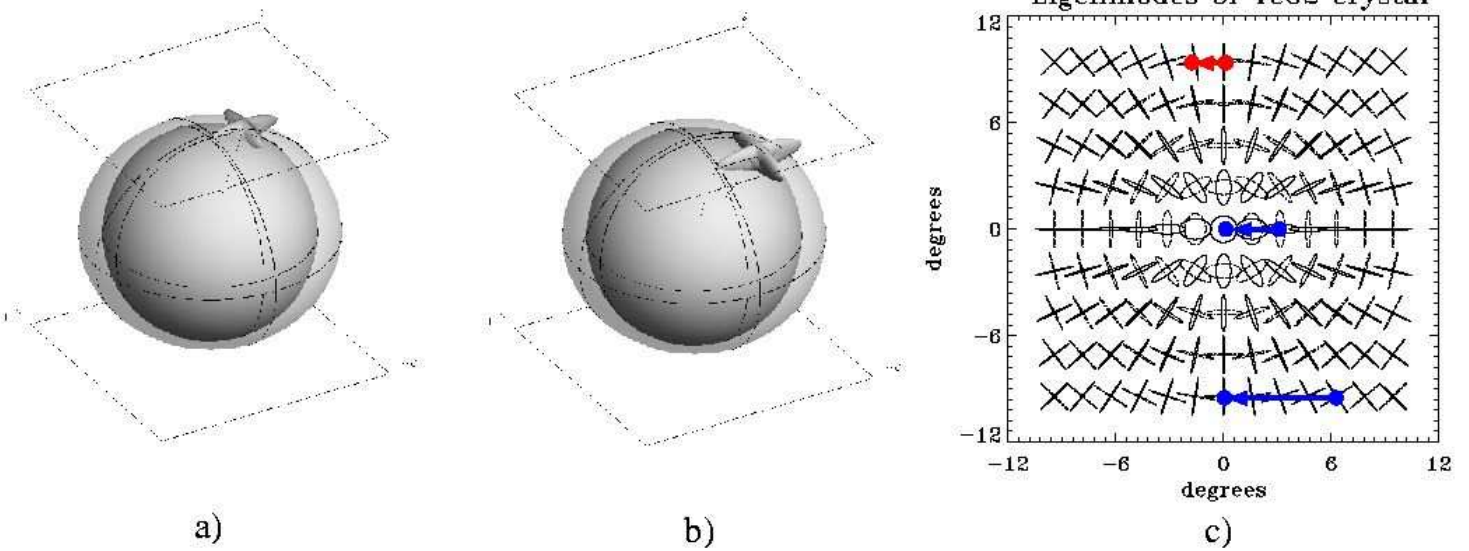


Figure 4: a) 3-D momentum space showing the tangentially phase-matched acousto-optic interaction around the z-axis with an exaggerated splitting due to optical activity and a corresponding exaggerated acoustic frequency.<sup>22</sup> b) Optically rotated acousto-optic interaction in TeO<sub>2</sub>. c) The eigen polarization of a TeO<sub>2</sub> crystal near the optic axis for a wavelength of 780 nm over a range of  $\pm 10$  degrees. The eigen polarization is circular near the optic axis and changes to linear polarization as the angle deviates by a few degrees away from the optic axis.

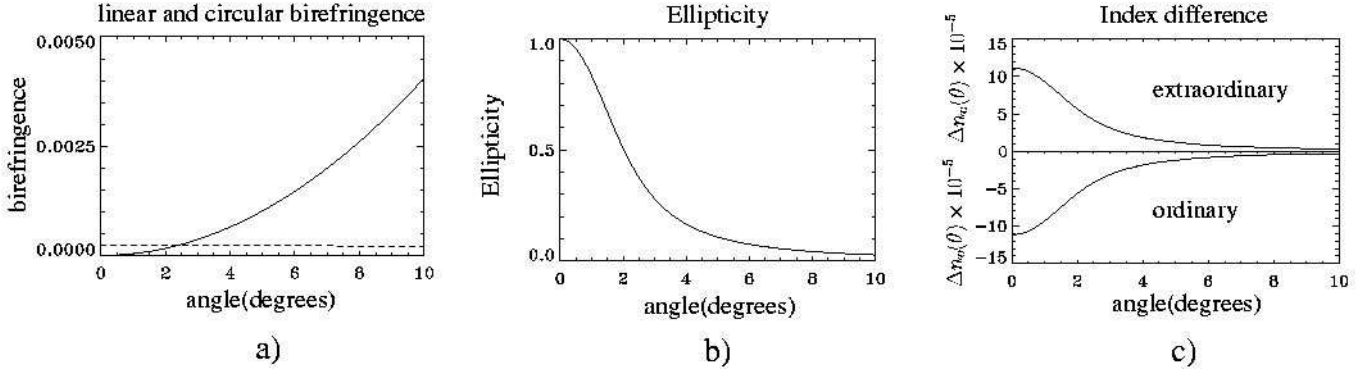


Figure 5: a) The solid line is the linear birefringence  $\Delta n_l$  and the dashed line is the circular birefringence  $\Delta n_c$  at 780 nm wavelength. b) The ellipticity  $\xi$  as a function of angle from the z-axis. c) The difference of the  $\text{TeO}_2$  indices of refraction when there is optical activity and when there is no optical activity as a function of an angle  $\theta$  from the z-axis.

fringent diffraction near the z-axis, since the acoustic slow-shear mode launched from the transducer can couple light from the outer extraordinary eigen surface to the inner ordinary eigen surface.<sup>24</sup> The momentum-matched interactions are illustrated by the intersections between the acoustic momentum surface centered at the  $\vec{k}_e$  vector of the incident light with the inner optical momentum surface, as illustrated in three-dimension in Figure 4 a), with an exaggerated optically active splitting and correspondingly increased acoustic frequency for illustrative clarity. Optical rotation is a rotation around the normal to the transducer that rotates to a plane with larger splitting between the eigen surfaces and thus requires a higher momentum matching frequency and correspondingly larger acoustic momentum as illustrated in Figure 4 b). Optical modes propagating near the z-axis have circular polarization eigenmodes, while propagation directions further from the z-axis, as illustrated in Figure 4 c), have eigenmodes that approach linear polarization for rotation of a few degrees away from the z-axis. Without optical rotation, an elliptically polarized incident wave diffracts to a circularly polarized eigenmode as shown in the middle part of Figure 4 c). With a few degrees of optical rotation, the incident and diffracted eigenmodes become nearly linear and a larger acoustic momentum is required for tangential on-axis diffraction as shown at bottom of Figure 4 c). The required acoustic momentum and its eigenmodes for the acoustically rotated AODs designed in section 4 are also illustrated in the upper part of Figure 4 c).

The  $\hat{o}$  and  $\hat{e}$  eigenmodes have circumferential and radial major axis orientations that are most easily expressed using spherical polar coordinates. Ellipticity ( $\xi$ ) is defined as the ratio of the major ( $a$ ) and minor ( $b$ ) axes ( $\xi = \frac{b}{a}$ ) of the polarization ellipse, giving  $\pm 1$  for circular polarization and 0 for linear polarization. For a propagating angle  $\theta$  away from the z-axis, the ellipticity of the incident and diffracted eigenmodes is given by<sup>26</sup>

$$\xi = \frac{\Delta n_c(\theta)}{\Delta n(\theta) + \Delta n_l(\theta)}, \quad (6)$$

where  $\Delta n(\theta) = \sqrt{[\Delta n_c(\theta)]^2 + [\Delta n_l(\theta)]^2}$  is the total birefringence at an angle  $\theta$  away from the z-axis,  $\Delta n_l(\theta) = n_e(\theta) - n_o \approx (n_e - n_o) \sin^2 \theta$  is the linear birefringence when optical activity is neglected, and  $\Delta n_c(\theta) \approx \frac{\rho_r \lambda}{\pi} \cos^2 \theta$  is the circular birefringence induced by optical activity

near the optical axis, where  $\rho_r$  is the optical rotatory power defined as the rotation angle of the linear polarization per unit length. The circular birefringence ( $\Delta n_c$ ) is dominant close to the z-axis, giving circular optical eigenmodes along the z-axis, while the linear birefringence ( $\Delta n_l$ ) dominates further away from the z-axis, eventually giving nearly linear optical eigenmodes polarization for more than 10 degrees away from the z-axis as shown in Figure 5 a). At 780 nm wavelength, the ellipticity is  $\pm 1$  along the z-axis, and decreases to 0.027 when the propagation direction is 10 degrees away from the z-axis as shown in the Figure 5 b). The optical activity changes the ordinary and extraordinary index of refraction around the z-axis. The difference between an ordinary index of refraction with optical activity and one without optical activity ( $n_o(\theta) - n_o$ ) and the extraordinary difference with and without optical activity for 780 nm wavelength are illustrated in Figure 5 c). Along the z-axis, the deformed ordinary index surface (or momentum surface,  $k = 2\pi n/\lambda$ ) is pushed in, and the extraordinary surface (or momentum surface) is dimpled out as shown in Figure 5 c).<sup>27</sup>

### 3 Feasibility demonstration using off-the-shelf devices

As an initial demonstration, we performed multi-color Doppler-free beamsteering with a 633 nm HeNe laser and a 532 nm Ar laser using two off-the-shelf, conventional AODs, as shown in Figure 6. The AODs are made of  $\text{TeO}_2$  crystals and are oriented by rotating about the acoustic  $\vec{K}_a$  vector (transducer normal) with a 10-degree optical-rotation angle away from the z-axis (which is found by observing the conoscopic pattern using converging light between crossed polarizers). The eigenmode polarization of the input optical wave is rotated about 6 degrees from the vertical axis and the eigenmode of the output optical wave is horizontally oriented. For this large optical rotation angle, the ellipticity of the eigenmodes is about 3%, so appropriately oriented linear polarizations will achieve about 97% coupling efficiency to the eigenmode. Figures 6 b) and c) show the bandshapes of the AOD for two different wavelengths (633 and 532nm), both of which satisfy the tangential phase-matching condition. The 3 dB bandwidth is 50 MHz (50-100MHz) for 633 nm light and 30 MHz (75-105MHz) for 532 nm light. There is an overlap of the bandshapes for both wavelengths that ranges from 75 to 100 MHz that will result in extra unwanted diffraction of the wrong wavelength.

We need to apply two frequencies (combined with an RF adder) to address a single spot with both wavelengths. We can compensate for the angular difference caused by the wavelength difference using two RF frequencies with a ratio given by the inverse wavelength ratio,  $\frac{f_1}{f_2} = \frac{\lambda_2}{\lambda_1}$ . The first AOD, which is driven by two frequencies (68 MHz and 80 MHz) and oriented with a Doppler-upshifting diffraction, was imaged onto a second, 90-degree rotated, Doppler-downshifting AOD driven by the same two frequencies, canceling the Doppler shift and giving a linear scan along a 45° tilted line. The 90-degree rotation places the angular scan from the first AOD in the plane of Bragg degeneracy of the second AOD to avoid bandwidth-restricting Bragg-mismatching effects.<sup>28</sup> With appropriate RF frequencies, Doppler-free overlapping diffracted spots are produced, as shown in Figure 6 d). However, undesired diffractions are also produced because the bandshape for the two wavelengths overlap in the RF frequency domain. One of our design goals is to get rid of these undesired diffractions thereby improving the achievable efficiency of the desired Doppler-compensated

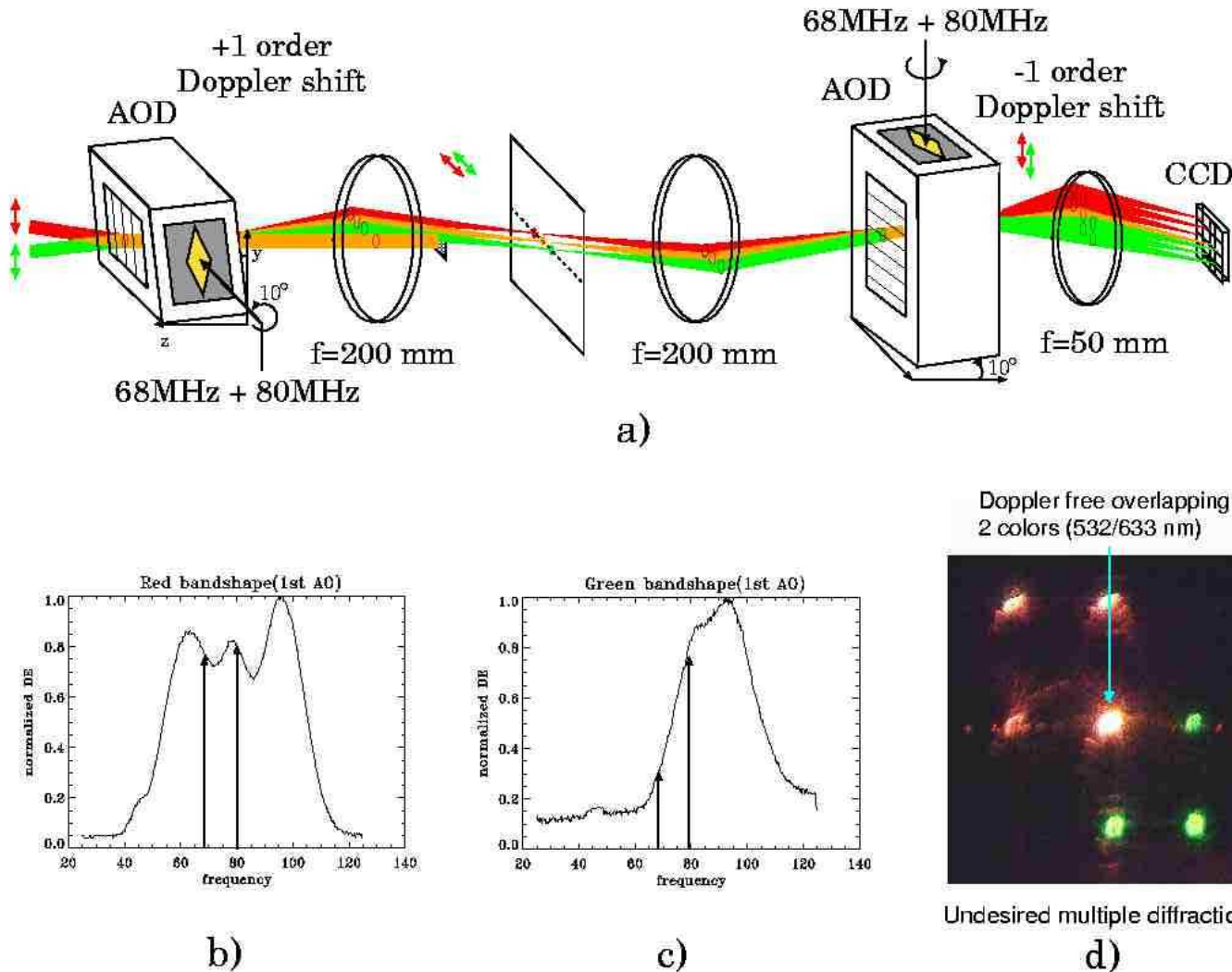


Figure 6: a) The experimental setup for demonstrating multi-color Doppler-free AO diffraction at two wavelengths (633 nm/532 nm). b) The RF bandshape of the  $\text{TeO}_2$  AOD at 633 nm using tangential phase matching geometry. c) The bandshape of the  $\text{TeO}_2$  AOD at 532 nm. The center frequency is higher at the shorter wavelength. d) The diffracted spots from the second AOD when driven by the two RF frequencies. The spot at the center is the deflected Doppler-free position where the two wavelengths overlap, while the other six are undesired cross diffractions.

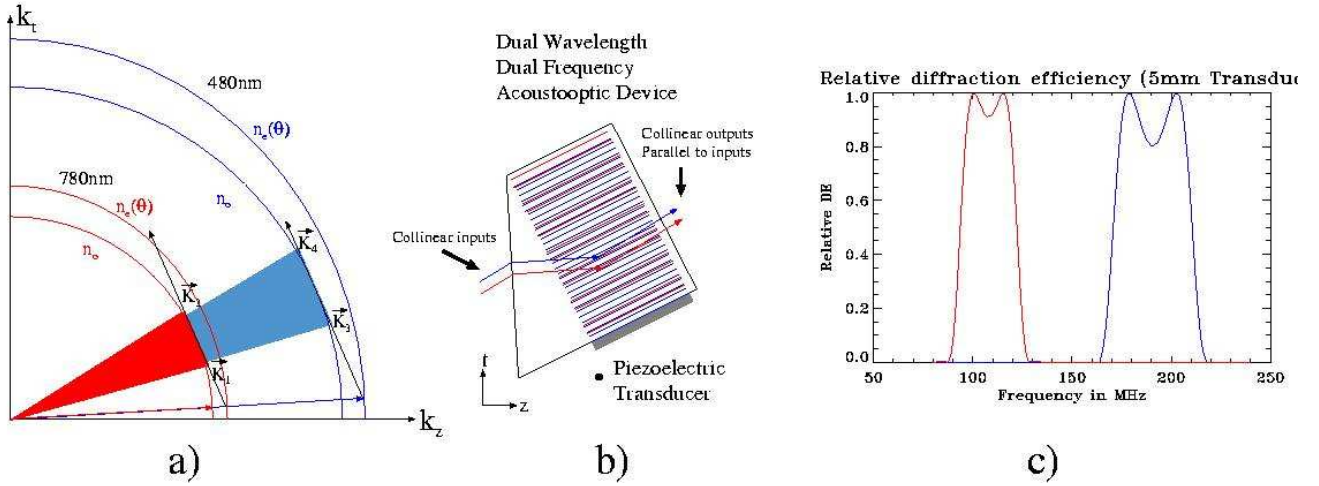


Figure 7: a) The momentum-space conceptual design of two-color spatially overlapping diffraction using anisotropic diffraction. b) Real-space design for the dual RF frequency input acousto-optic deflector for two-color diffraction. The AOD prism cut allows Bragg matching for parallel two-color inputs and yields an undeviated midband output for both colors. c) Dual bandshape for the two wavelengths are completely separated, enabling only a single overlapping Doppler-free deflection to be produced at both colors simultaneously.

diffractions and producing no unwanted extraneous terms.

## 4 Custom AOD Design

For this spatially-overlapping, two-color diffraction with the largest efficiency-bandwidth product, we employ tangentially phase-matched anisotropic diffraction for both wavelengths simultaneously, as shown schematically in Figure 7 a). The momentum surface for 480 nm is scaled up from that at 780 nm by the ratio of material wavelengths, and the actual splittings between the ordinary and extraordinary surfaces are exaggerated, but the basic geometry of the interaction is illustrated. The tangential geometry with maximal efficiency-bandwidth product is achieved when the correct polarization is incident at an angle onto the outer momentum surface for which the sum of  $\vec{k}_i + \vec{K}_a(f)$  skims tangentially across the inner momentum surface as the frequency is varied, so the phase mismatch is minimized across a wide bandwidth. The incident light at each color is tangentially diffracted by a range of non-overlapping acoustic frequencies towards a common overlapping region of output angles, and the transducer is lengthened compared to a conventional transducer to give suboctave bandwidth for each color. The full range of frequencies is contained in a single octave to avoid second harmonic diffractions and simplify the transducer impedance matching. For easy alignment of the system, a prism cut is utilized at the front face of the  $\text{TeO}_2$  crystal, which allows parallel collimated beams of both wavelengths to refract into the required Bragg-matching input angles, and at the output face to leave the diffracted beams undeviated at the midband for each color.

$\text{TeO}_2$  is an optically active, positive uniaxial crystal, which allows polarization-switching tangential birefringent diffraction at a convenient, low RF frequency. For conventional  $\text{TeO}_2$

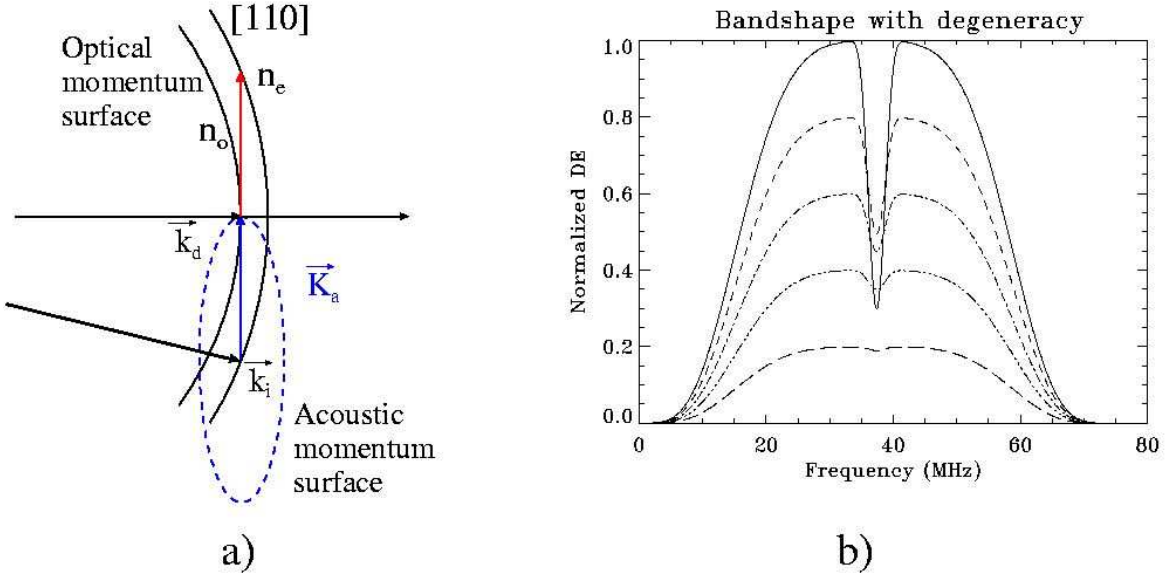


Figure 8: a) Optical momentum space showing midband degenerate diffraction. The size of acoustic momentum for the extraordinary outer momentum surface to the ordinary inner momentum surface for tangential birefringent diffraction is equal to the ordinary inner momentum surface to the extraordinary outer momentum surface diffraction due to the symmetry of optical momentum surface. b) As applied RF power increases, the ordinary inner momentum surface to the extraordinary outer momentum surface diffraction causes a dip in the middle of AO bandshape.

deflectors, the Bragg-matched interaction takes place near the z-axis of the crystal, where the slight splitting of the eigen surfaces due to optical activity is observable. For this dual-wavelength quantum computing application, the tangentially phase-matching frequency range for both wavelengths (780 nm/480 nm) was examined for both optical and acoustic rotation to find an optimal geometry. Various optically rotated planes of incidence were examined, and in these optically rotated planes of incidence, various acoustic rotations were analyzed to find the optimum crystal orientation. Optical rotations about the transducer face normal correspond to tilts out of the interaction plane while acoustic rotations correspond to tilts of the transducer in the plane of the AO interaction. The spacing between the inner and outer optical momentum surface increases with either optical or acoustic rotations, which requires larger RF frequencies for tangential phase matching.

Figure 8 a) shows a slice of the symmetric optical momentum surface and acoustic momentum  $\vec{K}_a$  satisfying tangential birefringent diffraction from the extraordinary outer momentum surface to the ordinary inner momentum surface. Due to the symmetry of this geometry, the acoustic momentum for tangential birefringent diffraction ( $\vec{K}_a$ ) near the central frequency satisfies the second order diffraction condition from the ordinary inner momentum surface to the extraordinary outer momentum surface, referred to as midband degeneracy.<sup>29</sup> As the applied RF power increases for higher diffraction efficiency, the midband degeneracy causes a large dip in the middle of the AO bandshape, as shown Figure 8 b).

With acoustic rotation, the midband degeneracy can be eliminated by breaking the symmetry of the second order diffraction, and the center frequency can be tuned as well.<sup>30,31</sup>

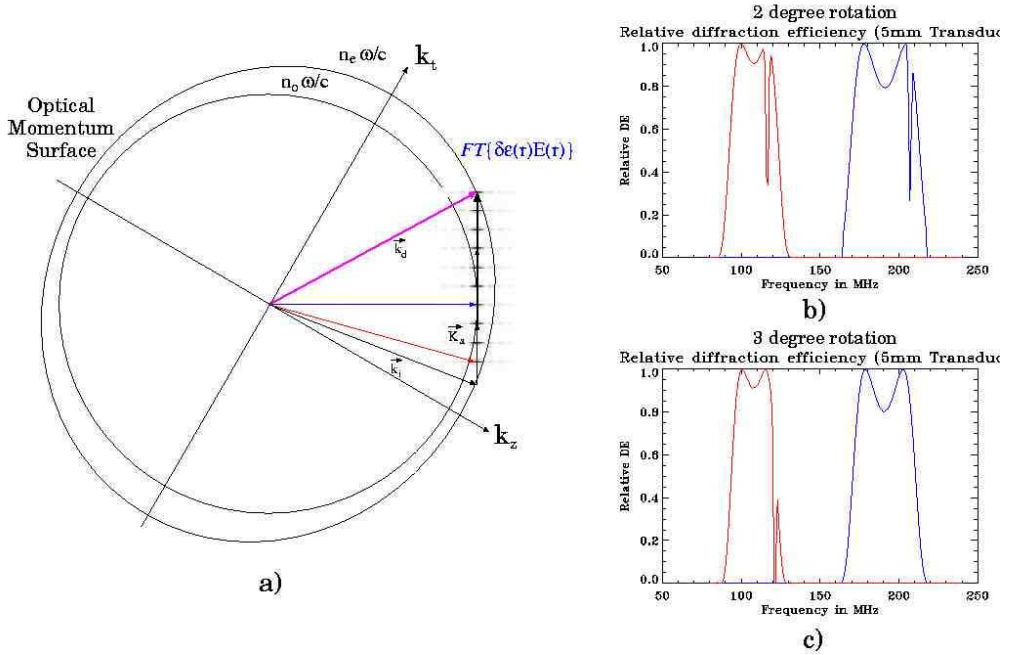


Figure 9: a) Optical momentum space showing degenerate double diffraction. As the applied frequency changes, the acoustic momentum vector changes its length proportionally and diffracts light from the extraordinary outer to the ordinary inner momentum surface. However, part of this diffracted light can rediffract from the inner to the outer optical momentum surface (degenerate diffraction) unless sufficient acoustic rotation away from the symmetric condition breaks the symmetry required for this double diffraction. b) With two degrees of acoustic rotation, the degenerate diffraction is inside our usable bandwidth. c) With three degrees of acoustic rotation, the degenerate diffraction dip is just outside our usable bandwidth.

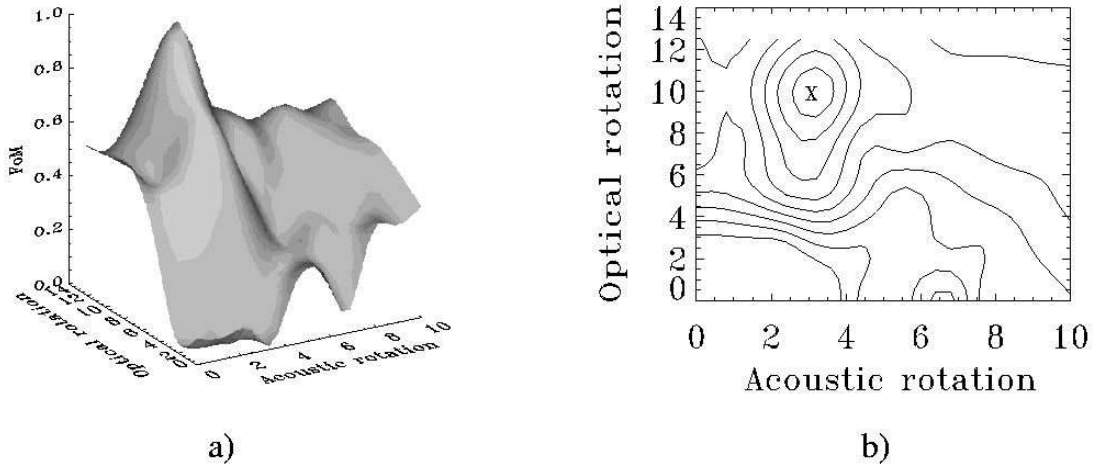


Figure 10: The figure-of-merit surface as a function of acoustic rotation and optical rotations in degrees. b) The topview of the figure-of-merit surface showing optimum point at 10-degree optical rotation and three-degree acoustic rotation.

With insufficient acoustic rotation the in-band degenerate diffraction causes a nonlinear dip in the RF bandshape of the tangential Bragg-matched diffraction bandshape, as shown in Figure 9 a), which is especially observable at high diffraction efficiency. For an insufficient amount of acoustic rotation, the acoustic momentum vector of length  $|\vec{K}_a| = 2\pi f/V_a$  can still satisfy the momentum-matching condition for light diffraction from the inner to outer optical momentum surface, thus rediffracting part of the diffracted light (a tangentially Bragg-matched diffraction from the outer to inner surface) as shown in Figure 9 a). With further acoustic rotation (up to three degrees in the 10 degree optically rotated plane of incidence), the in-band degenerate diffraction is completely outside the usable bandwidth at both wavelengths as shown in Figure 9 c).

However, acoustic rotation produces a large walk-off angle that increases at  $b_z=11$  times the rotation angle, which increases the required crystal volume. Also, the bandshapes for both wavelengths must be completely separated and fit within a one-octave bandwidth because over an octave the acoustic and transducer nonlinearities may yield undesired diffractions. This is just barely achievable in this case since the wavelength ratio is  $\frac{780}{480} = 1.62$ , thus the difference between center frequencies for 780 nm and 480 nm diffraction are inside one-octave bandwidth and the fractional bandwidth at both is about 0.2, making each bandwidth for 780 nm and 480 nm not to exceed an overall one-octave bandwidth. The high-frequency end is limited by the available transducer impedance-matching technology to about 230 MHz, and in addition the frequency dependence of the acoustic absorption (18dB/ $\mu$ s/GHz<sup>2</sup>) requires that high frequencies are avoided if high resolution is required.

Considering all these limitations, various optical and acoustic rotations were evaluated to find the optimized crystal orientation of the AOD in order to find a large bandwidth for both wavelengths (thus giving more resolvable spots) while minimizing the bandwidth in excess of an octave,  $BW_{\text{ovoctv}}$ , as well as the crystal size. A figure of merit that increases with the bandwidth at both 480 nm and 780 nm but is penalized for large crystal volume

and bandwidth in excess of an octave is given in Equation 7:

$$\text{Figure of Merit} = \frac{\text{BW}_{\text{blue}} + \text{BW}_{\text{red}} - \text{BW}_{\text{octv}}}{\text{CrystalVolume}} \cdot U_{\text{hflimit}} \cdot F_{\text{midgen}}, \quad (7)$$

where  $U_{\text{hflimit}}$  is a function representing the high frequency limit due to the constraints of the transducer impedance-matching technology (around 230 MHz), and  $F_{\text{midgen}}$  denotes a function penalizing a geometry with the degenerate diffraction inside the usable bandwidth. This figure of merit is plotted in Figure 10 as a function of optical and acoustic rotation angles and was used to choose an optimized device geometry. This shows that with a 10-degree optically rotated plane of incidence and three-degree acoustic rotation of the transducer face, the optimized performance is achieved. Figures 11 a) and b) show the bandshapes of the designed AOD for both wavelengths plotted in the angular domain. The bandshapes for both wavelengths are angularly overlapped and centered at 3 degrees. The 20 mm transducer is fully optimized to just fit within an octave bandwidth as limited by the red wavelength on the low frequency (angle) side and the blue wavelength on the high frequency (angle) side. The undesired diffraction from the second order acoustic nonlinearity or multiple diffraction is still inside the usable bandwidth for the 5 mm-long transducer (shown as vertical lines in Figure 11 b)), but the usable bandwidth is nearly the same as for the 20 mm-long transducer. Considering that the 20 mm transducer requires a much larger crystal and is much harder to impedance match over a full octave due to the large area and capacitance than the 5 mm transducer, we chose to use the 5 mm-long transducer. There is a decrease in diffraction efficiency in %/Watt (as shown in Equation 4) with the 5 mm transducer, but we can still expect more than 80% diffraction efficiency with sufficiently high RF power. The 480 nm wavelength is designed with a 1.0 dB ripple and the 780 nm with a 0.5 dB ripple, so that two cascaded devices will have 2dB/1dB ripple, respectively. Even though the 480 nm wavelength has a wider bandwidth than the 780 nm wavelength in the RF frequency domain, the angular scan range is smaller at 480 nm than 780 nm wavelength, as shown in Figure 11. Since our design goals are maximizing both the RF bandwidth and the angular overlap range for both wavelengths, the 480 nm wavelength was designed with more ripple (giving wider bandwidth) than was used at the 780 nm wavelength.

Once the transducer length  $L$  has been chosen, the height  $H$  can be selected in order to keep the full aperture  $A$  in the acoustic near field and minimize non-uniformities due to acoustic diffraction. The enormous out of plane acoustic curvature,  $b_t=52$ , scales the near-field distance for a rectangular transducer back to  $Z_0 = \frac{H^2}{b_t \Lambda_a}$  and  $H$  is usually chosen so that  $A < Z_0$  to maintain well-collimated acoustic column. Alternatively, a diamond or truncated diamond transducer can be used to apodize the acoustic propagation, thereby producing a more uniform acoustic field projection as shown in Figure 12 d), which is a projection of the 3-D propagated acoustic field. In the orthogonal Bragg plane, the sidelobes of the Bragg selectivity are lowered by the triangular apodization of the projection of the diamond, which lowers the Bragg mismatched crosstalk. We consider an 8mm×4mm diamond-shaped transducer as shown in Figure 12 a) as an alternative to a 5mm×3mm rectangular transducer with the same area and capacitance. The Fourier distribution of the diamond transducer acoustic wave, which is the amplitude weighting painted across the momentum surface (as illustrated in Figure 3 a)), is shown in Figure 12 b) along with the curved intersection between the optical and acoustic momentum surfaces at midband. The advantage of using

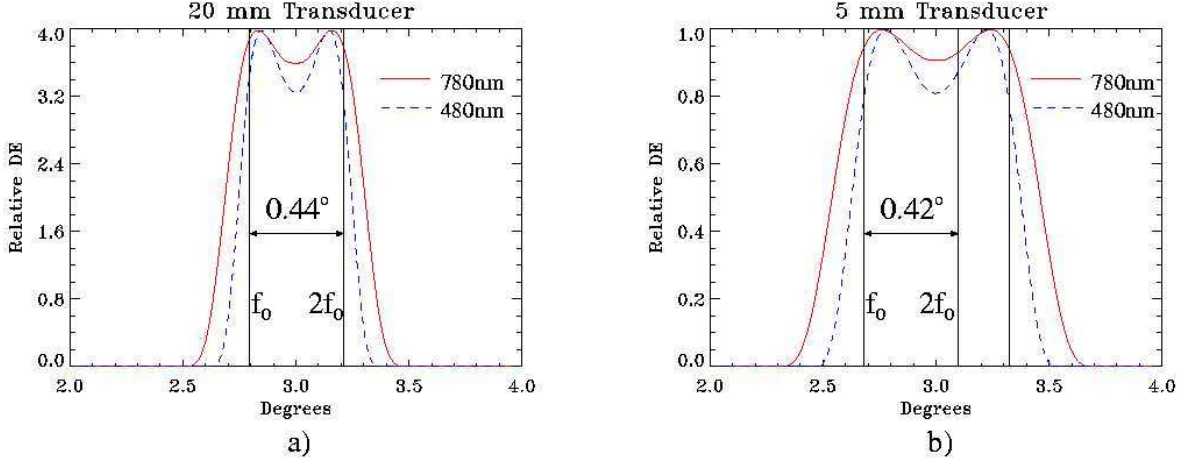


Figure 11: a) The bandshape of the designed AO device with a 20 mm transducer length shown in the angular domain and demonstrating good overlap between the two wavelengths (780/480 nm) and centered at three degrees (the acoustic rotation angle). 780 nm bandshape is plotted with solid line and 480 nm bandshape is plotted with dotted line. Octave bandwidth limits are delimited by the vertical lines. b) Since such a large transducer is difficult to impedance match, a smaller 5 mm-long transducer was evaluated and is shown to have wider bandwidth and angular scan width. However, the delineated octave bandwidth limit is about the same as the 20 mm transducer, although the efficiency is 4 times lower.

a diamond-shaped transducer over a rectangular transducer is the small amplitude of the in-plane first order sidelobe (-26 dB compared with -13 dB for the rectangular transducer). The in-plane uncertainty distribution of the diamond shaped transducer is  $\text{sinc}^4(k_z \frac{L_d}{4\pi})$ , giving an RF bandshape with a narrower 3 dB bandwidth and lower sidelobe compared with the rectangular transducer ( $\text{sinc}^2(k_z \frac{L_s}{2\pi})$ ) where  $L_d = 2L_s$ , as shown in Figure 12 c). Figure 12 d) shows an acoustic beam propagation simulation of the rectangular transducer and the diamond transducer corresponding to the projection of the three-dimension acoustic field as accumulated by the Bragg-matched read out laser. The diamond transducer has a more uniform acoustic intensity distribution near the transducer compared with the rectangular transducer. These nonuniformities will diffract light toward the vertical  $k_t$  dimension, producing vertical sidelobes, as also visible in the  $\vec{k}$ -space Bragg-matched loci shown in Figure 12 b).

The designed AOD uses a crystal about 1 cm long and 1.5 cm wide. The walk-off angle due to three degrees of acoustic rotation is 32 degrees, as shown in Figure 13 a). The front face has a 6.14-degree prism cut to satisfy the Bragg-matching condition of collinearly incident 780 nm and 480 nm beams. The upper face has a one-degree wedge to Bragg-mismatch acoustic wave reflections going back to the transducer. Figure 13 b) shows the 10-degree inclined front surface for optical rotation and the inclined diamond transducer electrodes. The piezoelectric transducer is oriented with the shear particle motion along the  $\bar{1}\bar{1}0$  axis and two transducers were implemented: an L=5 mm diamond and an L=8 mm truncated diamond transducer.

Unlike unrotated or isotropic AODs in which a single device can be rotated to Bragg match either the plus or minus Doppler order, for non-symmetric acoustically rotated devices,

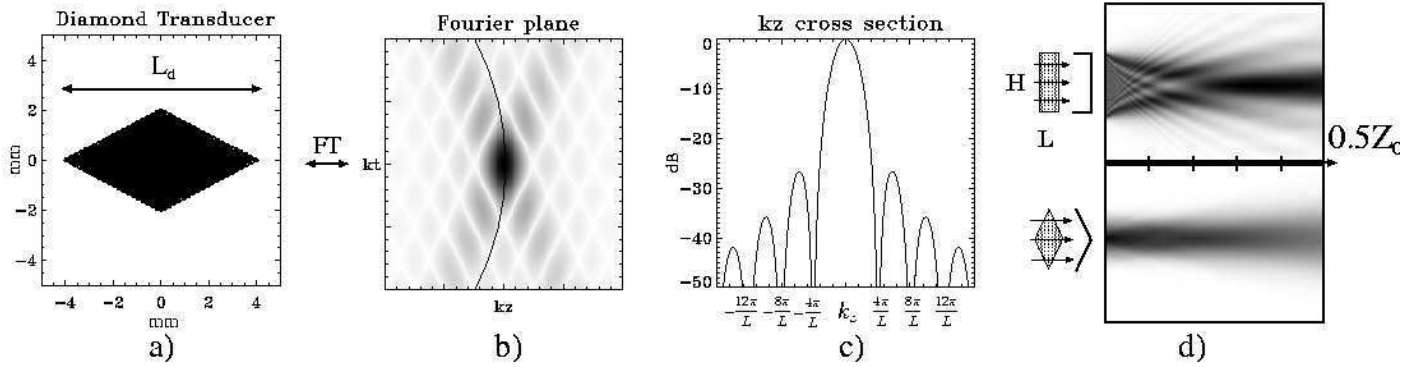


Figure 12: a) Diamond-shaped transducer with 8 mm length and 4 mm height. b) Fourier transform of diamond-shaped transducer and Bragg-matched loci due to the momentum surface intersections. c)  $k_z$ -dimensional cross section of the Fourier plane. d) Beam propagation of rectangular and diamond-shaped transducer.

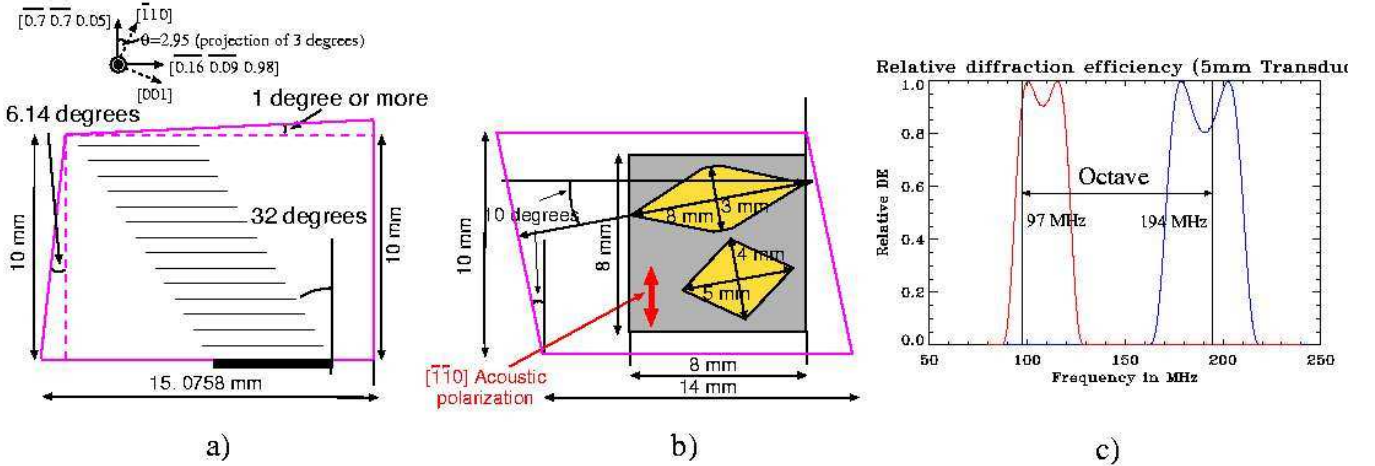


Figure 13: a) The top view of the designed AOD showing a prism wedge cut for optical input face and acoustic walk-off, b) The sideview of the designed AOD showing 10-degree optically rotated input face with two diamond-shaped transducer electrodes (5 mm and 75 % truncated 8 mm), c) The expected bandshape for 780 nm/480 nm with 5 mm transducer.

separate AODs need to be fabricated for Doppler upshifting and downshifting interactions in order to combine as a Doppler-compensated pair. For the AOD with the minus-order diffraction, we need to place the transducer at the upper face of the AOD crystal, as shown in Figure 13 a). The acoustic wave propagates exactly along the same path as in the plus-order device, but the direction of propagation is reversed to produce a minus-order Doppler shifted diffraction. For the 780/480 nm wavelengths, the AOD has 108/191 MHz center frequencies and 21/34 MHz bandwidths, as shown in Figure 13 c); thus the bandshapes (97-119 and 174-208 MHz) are widely separated and nearly contained within an octave bandwidth (97-194 MHz). The optical aperture is 10 mm in length and 3-4 mm in height, and the full aperture access time is 16  $\mu$ s, yielding a time-bandwidth product of 336 for 780 nm and 560 for 480 nm. For a circular beam with 4 mm  $1/e^2$  diameter, over 100 resolvable spots can be achieved with an access time of 4  $\mu$ s, which should allow a 32 qubits, one-dimensional array of well-resolved atoms to be rapidly addressed with low crosstalk for this quantum computing application. The cascaded AODs also work as two-dimensional scanner, although with a Doppler shift given by the sum or difference of the driving frequencies along the two axes. To address the two-dimensional array of atoms (32  $\times$  32), the Doppler shift can be pre-compensated by acousto-optic modulators (AOM) for each wavelength (780/480 nm) driven by the appropriate sum frequency.

## 5 Experimental results

In order to characterize the performance of our Doppler-free, dual-wavelength scanner, we first made bandshape and diffraction efficiency measurements of the AODs with collinear multi-wavelength laser beam inputs aligned at the Bragg angle. We used a 476 nm argon laser and 785 nm laser diode for our test light sources since modeling shows that these wavelengths are close enough to test the performance of devices originally designed for the 780/480 nm wavelengths.

### 5.1 Bandshape measurement

Both the 476 nm and the 785 nm beams with 4 mm diameter are collinearly incident on the AOD with a prism cut at the front face, so the beams refract into the crystal at two slightly different angles for appropriate Bragg matching designed to give 1 dB ripple at 480 nm and 0.5 dB ripple at 780 nm. The bandshapes are measured with a signal sweeping from 50 to 250 MHz. The applied RF chirp signal drives the AOD, which diffracts the collinearly incident light (785/476 nm) to the same range of diffracted angles (spatially overlapping in the Fourier plane). We placed an  $f=130$  mm aplanatic triplet lens after the AOD to focus the diffracted beam to a spot that changes its location with the applied RF chirp frequency. A 1 cm diameter detector head is placed at the Fourier plane to measure the diffraction efficiency as the signal generator sweeps in frequency. An oscilloscope records the time-varying diffraction efficiency to measure the AOD bandshapes. Figure 14 shows the measured bandshapes for both wavelengths, which are well-separated in the frequency domain as required for efficient dual frequency operation. Both bandshapes have usable bandwidths of about 30 MHz, which correspond to more than 100 resolvable spots for a 4

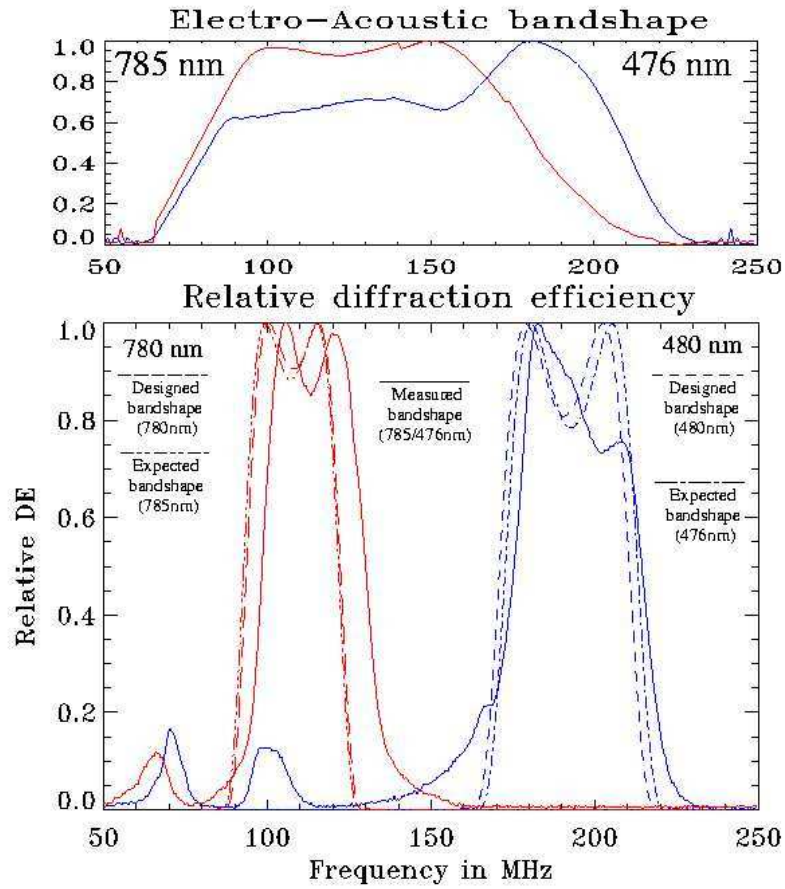


Figure 14: Comparison of the designed (780/480 nm) and measured (785/476 nm) bandshape of the fabricated AOD. Bandshapes for 780 nm and 480 nm wavelength are well-separated in the RF frequency domain and have around 30 MHz of bandwidth. Theoretical bandshape at 785/476 nm is also shown, which is down and up-shifted compared with the 780/480 nm design. The measured electro-acoustic bandshape at 785/476 nm is also shown.

mm diameter incident beam. As we rotate the AOD, we can observe the 0.5 dB ripple in the 780 nm bandshape. But for the 480 nm bandshape, the 1 dB ripple design is obscured since the bandshape appears to be limited by the high-frequency roll-off due to the transducer impedance matching. We observed this high frequency behavior by measuring the electro-acoustic bandshape, as shown in Figure 14. The electro-acoustic bandshape determines the acoustic power in the crystal at a given applied RF frequency by rotating to a perfectly Bragg-matching angle for each frequency. The expected bandshape for 785 nm is slightly downshifted from that designed at 780 nm, and the 476 nm is slightly upshifted compared to that designed for 480 nm, as shown in Figure 14. The slight frequency upshift of the measured bandshapes at both wavelengths indicates possible cut angle errors.

## 5.2 Doppler-free scanning

A linear, Doppler-free scanning experiment was performed with the fabricated AODs. Doppler-free scanning can be accomplished by cascading the diffracted light from the first AOD, upshifted by  $f$ , onto a second AOD driven by the same RF frequency,  $f$ , but oriented to downshift by  $f$ , yielding net zero Doppler-shift, but scanned by both devices. When the two AODs are in the same plane, canceling of the spatial scanning is avoided by having the acoustic wave (or images) counter propagate, which doubles the diffraction angle. But Bragg selectivity in the second AOD, due to the different diffraction angles in the first AOD, significantly reduce the cascaded bandwidth.<sup>27,28</sup> For this reason, we instead cross the two AODs with their acoustic wave propagating perpendicular, but with one AOD upshifting and the other downshifting, which achieves net Doppler-free scanning along the 45° bisector oriented vertically, as shown in Figure 15. The AOD crystals are placed near the edge of their housing for the plus and minus order AODs, so we can place the plus and minus AOD crystals right next to each other for Doppler-free cascade operation without an intervening telescopic imaging system. For our experiments, we did utilize a telescope with two  $f=100$  mm focal length achromatic lenses and a DC block. We placed our AODs in gimbal mounts with tilt (optical rotation) and rotation (Bragg rotation) motion, which are in turn mounted in a V-block to rotate the AODs by 45 degrees to give combined horizontal (or vertical) Doppler-free scanning. Figure 15 b) shows the Doppler-free y-scan captured by a Charged Coupled Device (CCD) when both AODs are driven by the same wideband chirp and illuminated by both 480 and 780 nm collimated incident light, demonstrating cascaded Doppler-free dual-wavelength AO scanner operation.

Figure 15 c) shows the overlapped two-color Doppler-free diffracted spot, achieved using two well-separated RF frequencies (100 and 180 MHz) with 10 dBm (10mW) RF power as combined using a power adder and amplified with a 20 dB gain-power amplifier giving 50-60% diffraction efficiency for each wavelength (780/480 nm). The added RF frequencies were then split into two arms using an RF power splitter to drive both of the AODs. The separated RF signals diffract each wavelength (780/480 nm) to the same location, but due to the well-separated bandshapes (95-115 MHz at 780 nm and 170-205 MHz at 480 nm), the 100 MHz signal only diffracts the 780 nm beam, and the 180 MHz only diffracts the 480 nm beam without any undesired crosstalk diffractions.

We set up a Mach-Zehnder interferometer with the undiffracted laser directly from the 785 nm laser diode as a reference beam, combined at a beamsplitter with the cascaded doubly

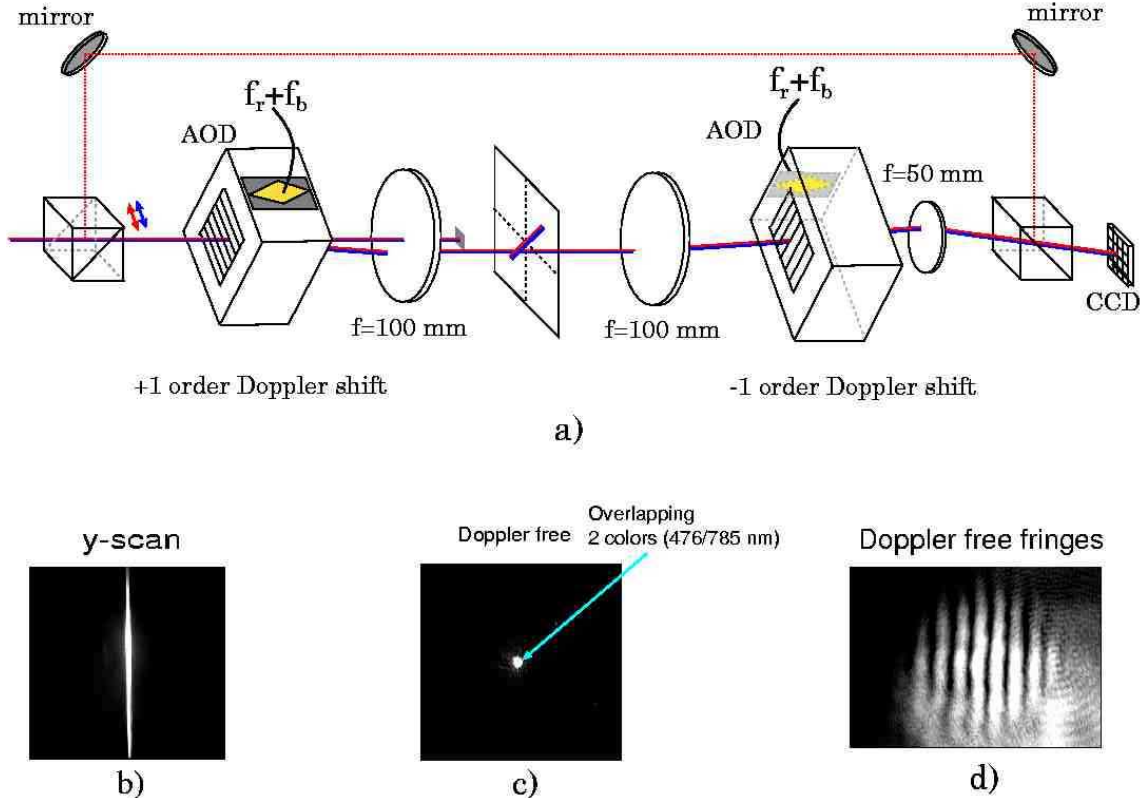


Figure 15: Experimental setup and dual-wavelength of Doppler-free scanner demonstration. a) The first AOD with positive Doppler-shifted diffracted light is imaged onto the second 90-degree-rotated AOD, which cancels the Doppler-shift with minus order diffraction when driven with the same frequency. b) The image of the one-dimensional Doppler-free scan (y-scan) is shown. c) Due to the frequency separation of the bandshapes for the two colors, there are no undesired diffractions when two different single RF frequencies (100/180 MHz) were applied to the AODs. d) Doppler-free operation was verified by the stationary interference pattern between the laser reference and the doubly diffracted beam.

diffracted beam, to verify that the diffracted spot is indeed Doppler-free. We observed static interference fringes, as shown in Figure 15 d), which shows that the scanning beam is not Doppler shifted as expected.

### 5.3 Small spot addressing

We need to build an optical system to address the  $^{87}\text{Rb}$  atoms trapped in closely spaced and tightly focused potential wells for Rydberg excitation. The size of the potential wells for the  $^{87}\text{Rb}$  atom trap is  $4 \mu\text{m}$  and the spacing between trapped atoms is only  $8 \mu\text{m}$ . For successful qubit addressing, the optical system should have diffraction-limited performance without any aberrations and small enough spots that crosstalk with the neighboring trapped atoms is negligible. We used a custom triplet lens that cancels chromatic aberrations and the large spherical aberrations induced by the thick vacuum chamber windows necessary for atom trapping and cooling (lens designed by Thad Walker, University of Wisconsin). The custom triplet lens works as a  $3.64\times$  demagnifier when used with an  $f=400$  mm collimation lens. To generate spots less than  $4 \mu\text{m}$  in diameter inside the vacuum chamber, we need to appropriately choose the size of the beam incident on the AOD, and the focal length of the Fourier lens after the Doppler-free AOD scanning system. The designed heights of the two transducers are either 3 mm or 4 mm for each AOD, which limit the maximum size of the spot illuminating the AODs since plano-convex cylinder lenses should be avoided when trying to maintain diffraction limited performance. If the Gaussian beam incident on the AOD scanner has a diameter  $D=3$  mm, we need to use an  $f=42$  mm Fourier lens to generate a  $13.9 \mu\text{m}$  focused spot for 780 nm and an  $8.6 \mu\text{m}$  focused spot for 480 nm, which are ideally then demagnified to  $3.8 \mu\text{m}$  (780 nm) and  $2.4 \mu\text{m}$  (480 nm) focused spots by the custom triplet in combination with the  $f=400$  mm collimation lens.

We experimentally demonstrated the required performance of the Doppler-free AOD scanner to address the closely-separated ( $8 \mu\text{m}$ ) atoms in the quantum information processor with minimal unwanted crosstalk with neighboring atoms. Figure 16 a) shows the experimental setup for examining the wavefront quality and resulting focal spots size of our Doppler-free AOD scanner. The Doppler-compensating, 90-degree-crossed AODs were cascaded using a telescope imaging system ( $f=100$  mm achromatic doublet lenses). The incident Gaussian beam had  $2.0 \text{ mm } 1/e^2$  diameter clipped by a 2 mm circular aperture. The Fourier lens, after successive diffraction by both AODs, had a 24 mm focal length. A knife edge beam profiler was used to measure  $1/e^2$  full width of the focused spots (785/476 nm) as  $21.4 \mu\text{m}$  for 785 nm and  $15.2 \mu\text{m}$  for 476 nm. The  $f=400$  mm lens collimated the focused spot, and the  $f=110$  mm custom triplet lens demagnified the focused spots to  $4.2 \mu\text{m}$  (476 nm) and  $5.9 \mu\text{m}$  (785 nm)  $1/e^2$  diameter after the 10 mm thick vacuum window. The demagnification ratio is around 3.62 for both wavelengths. We also placed a 750 mm focal length Fourier lens after the cascaded AODs to examine if there is any noticeable distortion in the spot shape after cascaded diffraction from the AODs. The captured spot images in the inset of Figures 16 b) and c) show the magnified diffracted spots without significant aberrations.

Without aberrations and with uniform illumination of the device aperture, the number of resolvable spots are given by the time-bandwidth product,  $T \cdot B$ . As shown in Figure 14, the bandwidth of the fabricated AODs is about 30 MHz. However, when the plus and minus AODs were cascaded, the cascaded bandwidth was reduced to about 15 MHz. The

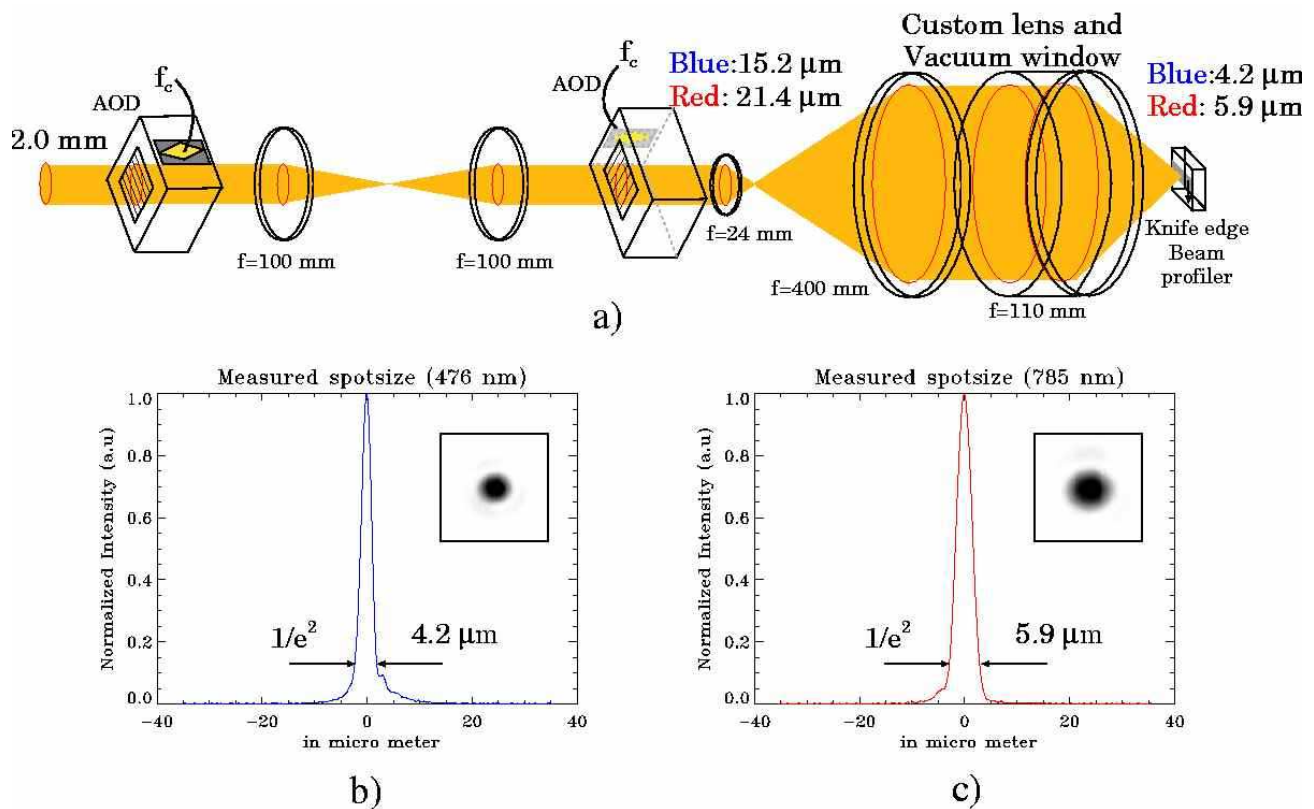


Figure 16: a) Experimental setup for measuring the achievable spotsize of the cascaded AODs and optical system. b)  $4.2 \mu\text{m}$   $1/e^2$  intensity width of the measured spot at 476 nm wavelength. The inset shows a magnified spot image produced by a 750 mm focal length lens placed after the cascaded AODs that is captured by a CCD camera and shows low aberration. c)  $5.9 \mu\text{m}$   $1/e^2$  intensity width of the measured spot at 785 nm wavelength also shows low aberration at 785 nm wavelength.

QIP application requires  $\mu\text{s}$  scale spot addressing and switching time in order to perform many operations before the decoherence time. Assuming a  $2\ \mu\text{s}$  required switching time, which can be achieved using a 1.2 mm beam, the number of resolvable spots of the one-dimensional Doppler-free scanner is  $T \cdot B = 30$ . This indicates that we can address 30 Rydberg atomic qubits, or 10 qubits with an over-resolving factor of three for well resolved one-dimensional scanning. For two-dimensional scanning, we can use the crossed cascaded AODs with Doppler pre-compensation achieved using AOMs for both wavelengths. We can expect to address well resolved  $10 \times 10$  two-dimensional array of atoms with  $2\ \mu\text{s}$  switching time.

## 6 Conclusion

We have presented the design, experimental demonstration and characterization of a novel AOD, which simultaneously diffracts two incident optical wavelengths (780 nm and 480 nm) with the exact same diffraction angle by using two proportional frequencies for application in two-photon addressing of an array of trapped  $^{87}\text{Rb}$  atoms. The AOD is designed to use two well-separated Bragg-matched frequency subbands within an overall octave RF bandwidth. The optimum crystal orientation with both optical and acoustic rotation was found by investigating the details of the interaction in momentum space. A prism cut was implemented at the optical input surface to allow collinearly incident input beams (780 nm/480 nm) to refract into the appropriate Bragg-matched incident angles and to give parallel input and diffracted output beams at midband, which simplifies the alignment on an optical rail. We can address an array of 30 well-resolved atoms rapidly ( $2\ \mu\text{s}$ ) with the designed AOD at both 780 and 480 nm, with the diffracted spots precisely overlapped in the Fourier plane. The wavefront quality of the cascaded AOD scanner was examined by observing the focused spots after optical imaging with an optimized low aberration system through a thick vacuum window. For addressing two-dimensional arrays with crossed AODs, we expect to be able to address  $10 \times 10$  arrays of atoms for QIP application by using Doppler pre-compensation with an acousto-optic frequency shifter. In a subsequent paper, we will show how to simultaneously address multiple spots without crosstalk using a new cascaded AOD design.

For the optimum performance of the cascaded AODs, as well as for addressing the atoms with the desired polarizations, we need to be able to manipulate the state of polarization for both wavelengths simultaneously incident on the AOD to match the crystal eigenmodes and to transform the diffracted output polarization (which varies slightly with frequency) into the required polarization for the next stage. In a companion paper, we will describe the design of bichromatic waveplates that transform wavelength dependent eigenmode polarizations for cascaded AODs and another bichromatic waveplate to generate the required polarizations for Rydberg excitation after the cascaded AODs.

## Acknowledgements

The authors gratefully acknowledge the support of the National Science Foundation (NSF) ITR program and Warren Seale from NEOS technology for helpful discussions about fabricating these AODs. This work was supported by the NSF (grant # PHY-0205236) and

ARO-DTO (contract # DAAD19-02-1-0083).

## References

- [1] M. A. Nielsen and I. L. Chuang, *Quantum Computation and Quantum Information* (Cambridge University Press, Cambridge, U.K., 2000).
- [2] P. W. Shor, “Polynomial-time algorithms for prime factorization and discrete logarithms on a quantum computer,” *Soc. for Indust. and Appl. Math. J. on Comput.* **26**(5), 1484–1509 (1997).
- [3] L. K. Grover, “Quantum mechanics helps in searching for a needle in a haystack,” *Phys. Rev. Lett.* **79**(2), 325–328 (1997).
- [4] L. M. K. Vandersypen, M. Steffen, G. Breyta, C. S. Yannoni, M. H. Sherwood and I. L. Chuang, “Experimental realization of Shor’s quantum factoring algorithm using nuclear magnetic resonance,” *Nature* **414**, 883–887 (2001).
- [5] D. Leibfried, R. Blatt, C. Monroe and D. Wineland, “Quantum dynamics of single trapped ions,” *Rev. Mod. Phys.* **75**, 281–324 (2003).
- [6] J. H. Plantenberg, P. C. de Groot, C. J. P. M. Harmans and J. E. Mooij, “Demonstration of controlled-NOT quantum gates on a pair of superconducting quantum bits,” *Nature* **447**, 836–839 (2007).
- [7] T. C. Ralph, “Quantum optical systems for the implementation of quantum information processing,” *Rep. Prog. Phys.* **69**, 853–898 (2006).
- [8] D. Schrader, I. Dotsenko, M. Khudaverdyan and Y. Miroshnychenko, “Neutral atom quantum register,” *Phys. Rev. Lett.* **93**, 150501 (2004).
- [9] M. P. A. Jones, J. Beugnon, A. Gaëtan, J. Zhang, G. Messin, A. Browaeys and P. Grangier, “Fast quantum state control of a single trapped neutral atom,” *Phys. Rev. A* **75**, 040301(R) (2007).
- [10] D. D. Yavuz, P. B. Kulatunga, E. Urban, T. A. Johnson, N. Proite, T. Henage, T. G. Walker and M. Saffman, “Fast Ground State Manipulation of Neutral Atoms in Microscopic Optical Traps,” *Phys. Rev. Lett.* **96**, 063001 (2006).
- [11] G. K. Brennen, C. M. Caves, P. S. Jessen and I. H. Deutsch, “Quantum logic gates in optical lattices,” *Phys. Rev. Lett.* **82**, 1060–1063 (1999).
- [12] D. Jaksch, J. I. Cirac, P. Zoller, S. L. Rolston, R. Côté and M. D. Lukin, “Fast Quantum Gates for Neutral Atoms,” *Phys. Rev. Lett.* **85**, 2208–2211 (2000).
- [13] M. Saffman and T. G. Walker, “Analysis of a quantum logic device based on dipole-dipole interactions of optically trapped Rydberg atoms,” *Phys. Rev. A* **72**, 022347 (2005).

- [14] T. A. Johnson, E. Urban, T. Henage, L. Isenhower, D. D. Yavuz, T. G. Walker and M. Saffman, “Rabi flopping between ground and Rydberg states with dipole-dipole atomic interactions,” Submitted to Phys. Rev. Lett. (2007).
- [15] X. Wang, D. Wilson, R. Muller and D. Psaltis, “Liquid crystal blazed grating beam deflector,” Appl. Opt. **39**(35), 6545–6555 (2000).
- [16] L. Sun, J. Kim, C. Jang, D. An, X. Lu, Q. Zhou, J. M. Taboada and R. T. Chen, *Polymeric waveguide prism-based electro-optic beam deflector*, Opt. Eng. **40**, 1217–1222 (2001).
- [17] L. Y. Lin, E. L. Goldstein, J. M Simmona and R. W. Tkach, “Free-space micromachined optical switches with submillisecond switching time for large-scale optical cross connects,” IEEE Photon. Technol. Lett. **10**, 525–527 (1998).
- [18] C. Kim, C. Knoernschild, B. Liu and J. Kim, “Design and Characterization of MEMS Micromirrors for Ion-Trap Quantum Computation,” IEEE J. Quantum Electron. **13**(2), 322–329 (2007).
- [19] F. W. Freyre, “Zero frequency shift Bragg cell beam deflection and translation,” Appl. Opt. **20**(22), 3896 (1981).
- [20] R. T. Weverka, K. Wagner, R. R. McLeod, K. Wu and C. Garvin, “Low-Loss Acousto-Optic Photonic Switch,” in *Acousto-Optic Signal Processing*, N. J. Berg and J. H. Peligrino, eds. (Marcel Dekker, 1996), pp 479–573.
- [21] A. Yariv and P. Yeh, *Optical Waves in Crystals* (Wiley-Interscience, New York, N.Y., 2003).
- [22] R. McLeod, “Spectral-Domain Analysis and Design of Three-Dimensional Optical Switching and Computing Systems,” Ph.D., dissertation (University of Colorado, Boulder, Colo., 1995).
- [23] R. Mcleod, K. Wu, K. Wagner and R. T. Weverka, “Acousto-optic photonic crossbar switch,” Appl. Opt. **35**(32), 6331–6353 (1996).
- [24] N. Uchida, “Optical properties of Single-Crystal Paratellurite( $\text{TeO}_2$ ),” Phys. Rev. B **4**, 3736–3745 (1971).
- [25] B. A. Auld, *Acoustic Fields and Waves in Solids* (John Wiley and Sons, New York, N.Y., 1973).
- [26] J. Xu and R. Stroud, *Acousto-Optic Devices* (Wiley-Interscience, New York, N.Y., 1992).
- [27] A. Fukumoto, M. Kawabuchi and H. Hayami, “Polarization considerations in the operation of an two-dimensional  $\text{TeO}_2$  abnormal Bragg deflector,” Appl. Opt. **14**(4), 812–813 (1975).
- [28] P. S. Guilfoyle, “Problems in two dimensions,” Proc. SPIE **341**, 199–208 (1982).

- [29] A. W. Warner, D. L. White and W. A. Bonner, “Acousto-optic light deflectors using optical activity in paratellurite,” *J. of Appl. Phys.* **43**(11), 4489–4495 (1972).
- [30] T. Yano, M. Kawabuchi, A. Fukumoto and A. Watanabe, “ $\text{TeO}_2$  anisotropic Bragg light deflector without midband degeneracy,” *Appl. Opt.* **26**(12), 689–691 (1975).
- [31] P. Maak, L. Jakab, A. Barosci and P. Richter, “Improved design method for acousto-optic light deflectors,” *Opt. Commun.* **172**(1), 297–324 (1999).